



# Preferential heteroatom substitution into $\text{ZnIn}_2\text{S}_4$ nanosheets boosts photocatalytic hydrogen production

Palagiri Bhavani<sup>a</sup>, Shanmugasundaram Kamalakannan<sup>b</sup>, D. Praveen Kumar<sup>c</sup>, Hyung Chul Ham<sup>b,\*</sup>, Young-Kwon Park<sup>a,\*</sup>, Wooyul Kim<sup>d,\*</sup>

<sup>a</sup> School of Environmental Engineering, College of Urban Science, University of Seoul, 163 Seoulsiripdaero, Dongdaemun-gu, Seoul 02504, Republic of Korea

<sup>b</sup> Department of Chemical Engineering, Inha University, Incheon 22212, Republic of Korea

<sup>c</sup> Department of Chemistry, Yonsei University, 50 Yonsei-ro, Seodaemun-gu, Seoul 03722, Republic of Korea

<sup>d</sup> Department of Energy Engineering/KENTECH Institute for Environmental and Climate Technology, Korea Institute of Energy Technology (KENTECH), Naju 58330, Republic of Korea

## ARTICLE INFO

### Keywords:

$\text{ZnIn}_2\text{S}_4$

Nanosheet

Preferential substitution

Photocatalysis

$\text{H}_2$  evolution

## ABSTRACT

Interior modification through preferential substitution of heteroatoms in 2D materials can rescue surface reactive sites for enhanced charge kinetics and photo-activity. Here, Ru and Ni heteroatoms were successfully incorporated in  $\text{ZnIn}_2\text{S}_4$  (ZIS) nanosheets via a simple hydrothermal technique. Ru-ZIS photocatalysts exhibited improved photo-water splitting activity ( $26,400 \mu\text{mol} \cdot \text{h}^{-1} \cdot \text{g}^{-1}$ ) and good stability than that of Ni-ZIS and pristine ZIS under simulated sunlight, which may be related to the increase in reactive sites with Ru substitution, optimized adsorption-free energy of the reaction intermediates and charge kinetics. Ru substitution influenced Zn site availability and thus coordinated bonding with surrounding S ions. Ru-ZIS showed excellent hydrogen evolution performance and minimal change in Gibbs free energy ( $\Delta G_{\text{H}}$ ,  $\sim 0$  eV). By analyzing the density of states, both Ru and S sites had greater  $\text{H}^*$  intermediate absorption abilities. This study elaborates on the effect of preferential heteroatom substitution on photocatalytic performance and has widespread applications.

## 1. Introduction

Facile fuel energy consumption has increased greatly, resulting in tremendous atmospheric and environmental pollution, and the rapid depletion of facile fuel stores [1,2]. Because of these issues, hydrogen ( $\text{H}_2$ ) energy has gained wide interest from the research community as an alternative clean energy source with exceptional calorific value and abundant reserves [3,4].  $\text{H}_2$  fuel production through photocatalysis is a pollution-free technique operating under ambient conditions and abundant solar light. Photocatalysis is considered the most efficient and sustainable technique for converting chemical energy via solar energy [5]. The photocatalytic activity of such a system is driven by high visible light absorption, charge separation, and photo-induced electron transfer to the surface [6,7]. Numerous studies have investigated the development of efficient photocatalysts. Unfortunately, most photocatalysts have limited visible light absorption/solar light harvesting capabilities, restricting their industrial implementation [8].

The 2D-layered ternary bimetal chalcogenide-based semiconductor  $\text{ZnIn}_2\text{S}_4$  (ZIS) has emerged in various photocatalytic applications owing

to its environmental safety, tunable energy band gap (2.06–2.85 eV), and chemical stability [9,10]. However, the photo-activity of ZIS is severely restricted by its rapid charge recombination and poor photo-generated electron acceleration capacity, resulting in low photo-activity and stability [11,12]. The spatial separation of photo-induced charge pairs during the photocatalytic process is essential for enhancing  $\text{H}_2$  evolution rates. This can be achieved through various strategies, such as morphology regulation, heterojunction surface modification, doping engineering, defect engineering, and many others [13–16]. Interstitial doping engineering represents an efficient method of improving charge pair separation and charge dynamics by altering the optical band gap and electronic structure at the atomic level, and has shown greatly improved photocatalytic performance compared with other modification strategies. Various studies have shown that doping with metal ions, such as transition metals (Cu, Ni) [13,17,18] and precious elements (Pd, Au) [19,20], can greatly improve photocatalytic activity by acting on the nanoscale Schottky barrier heterojunction and localized surface plasmon resonance [21]. Among these, ruthenium (Ru) is considered an essential industrial metal in

\* Corresponding authors.

E-mail addresses: [ham.hyungchul@inha.ac.kr](mailto:ham.hyungchul@inha.ac.kr) (H.C. Ham), [catalica@uos.ac.kr](mailto:catalica@uos.ac.kr) (Y.-K. Park), [wkim@kentech.ac.kr](mailto:wkim@kentech.ac.kr) (W. Kim).

<https://doi.org/10.1016/j.apcatb.2024.124154>

Received 13 February 2024; Received in revised form 21 April 2024; Accepted 3 May 2024

Available online 8 May 2024

0926-3373/© 2024 Elsevier B.V. All rights are reserved, including those for text and data mining, AI training, and similar technologies.

photocatalysis, owing to its cheap production among the platinum group elements. Ru showed greater performance in  $H_2$  evolution compared to Pt because the Ru-H energy band gap is relatively narrower than that of Pt-H, as evidenced by efficient  $H^+$  generation and intermediate absorption abilities [22]. Ru doping of the photocatalyst can greatly suppress charge recombination, modify the energy band gap and potentials, and alter the local electronic configuration, leading to superior visible light absorption [23–28]. The vacant f-orbital in Ru atoms introduces intermediate-to-low energy levels, further modifying the visible light harnessing capacity [29]. The transition element Ni is an excellent reference material owing to its cheap price, abundance, and superior capabilities of absorbing water molecules and hydroxyl intermediates [30]. Building on their different advantages, a photocatalytic system employing various heteroatom dopant materials may efficiently optimize the local coordination of reactive sites, promote structural stability, enhance visible light absorption, reduce charge acceleration length, and ultimately improve photocatalytic activity.

Using a doping engineering-based approach, we assessed the influence of preferential heteroatom (Ru/Ni) substitution on photocatalytic activity in 2D ZIS (Ru/Ni-ZIS) nanosheets prepared through facile one-pot hydrothermal synthesis. Interior modification of the Ru-ZIS photocatalysts improved their photocatalytic water-splitting activity and chemical stability through the synergetic interaction of Ru-S with photocatalytic intermediates, greatly improving visible light absorption, photo-excited charge acceleration towards water dissociation, and ultimately  $H_2$  evolution rates. This study confirmed that interstitial Ru doping at Zn sites enhanced photo-activity compared to In interstitial doping, specifically because Ru easily replaces Zn on the surface of  $[ZnS]_4$  and then bonds with surrounding S ions, which have greater intermediate absorption ability. Our study elaborates on the advantages of single-component catalyst modifications in photocatalysis.

## 2. Experimental

### 2.1. Materials

This study mainly employed zinc nitrate ( $Zn(NO_3)_2 \cdot 6 H_2O$ , 98.0%, Sigma Aldrich), indium chloride ( $InCl_3$ , 98.0%, Sigma Aldrich), thioacetamide ( $CH_3CSNH_2$ , 98.0%, Wako), nickel nitrate ( $Ni(NO_3)_2 \cdot 6 H_2O$ , 99.99%, Sigma Aldrich), ruthenium chloride ( $RuCl_3 \cdot H_2O$ , NA, Sigma Aldrich), and ethanol ( $C_2H_5OH$ , Duksan). All raw chemicals were used without further purification.

### 2.2. Synthesis of $ZnIn_2S_4$ nanosheets

ZIS nanosheets were synthesized as previously described (Scheme 1) [31]. Briefly, 0.5 mmol zinc acetate dihydrate ( $ZnC_4H_6O_4$ ), 0.98 mmol

indium chloride ( $InCl_3$ ), and 2.05 mmol thioacetamide ( $C_2H_5NS$ ) were mixed in 60 mL of deionized water with vigorous stirring over 1 h. The uniformly dissolved solution was placed in a Teflon-lined Stainless-Steel autoclave and incubated at 220 °C for 36 h. The autoclave was left to cool to ambient temperature before the yellow precipitate was washed several times with deionized water and ethanol to remove impurities. The final solid yellow product was dried overnight at 80 °C for further usage.

### 2.3. Synthesis of Ru/Ni-doped $ZnIn_2S_4$ nanosheets

Following the same method as in Section 2.2, we added varying amounts of Ru precursor (0.05, 0.10, 0.15, 0.02, 0.225, or 0.25 mmol) prior to hydrothermal treatment, and named the resulting materials RZ-0.05, RZ-0.10, RZ-0.15, RZ-0.02, RZ-0.225, and RZ-0.25, respectively. For comparison, we prepared Ni-doped ZIS (Ni-ZIS, 0.10 mmol Ni) using the same process.

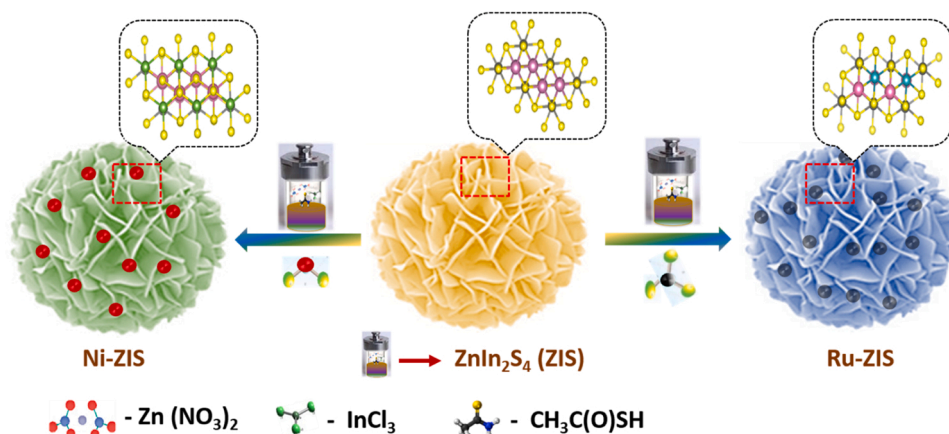
### 2.4. Characterization of photocatalysts

Powder X-ray diffraction (XRD) was performed to analyze the structures of the synthesized materials using a Rigaku D/MAX-IIIIC Advance X-ray diffractometer, with Cu  $K\alpha$  as X-ray source. Optical properties were obtained using diffuse UV-Vis reflectance spectra (UV-1800, SHIMADZU, Kyoto, Japan). The chemical composition and status of each material was analyzed using X-ray photoelectron spectroscopy (XPS, ESCALAB 250) with a 15 kV/150 W monochromated Al  $K\alpha$  X-ray source. Material morphologies and compositions were examined using field emission scanning electron microscopy (FESEM; SU8010, HITACHI) equipped with an energy dispersive spectrometer (EDS). High-resolution transmission electron microscopy with Cs corrector (STEM) imaging of microstructural properties was performed using a NEOARM JEOL JEM-ARM 200 F instrument at an accelerating voltage of 200 kV. A Hitachi F-7000 fluorescence spectrometer was used to record the room-temperature photoluminescence (PL) spectra of the prepared photocatalysts. For the time-resolved PL (TR-PL) analysis, the synthesized materials were excited by the second harmonic (355 nm) of a cavity-dumped oscillator (Mira/Pulse Switch, Coherent, 1 MHz, 710 nm, 150 fs).

The detailed experimental procedures for photocatalytic  $H_2$  production and photoelectrochemical measurements are provided in the [Supplementary Material](#).

### 2.5. Computational details

We used the Vienna Ab-initio Simulation Program (VASP) to perform all periodic density functional theory calculations. Total energy was



Scheme 1. Synthesis of ZIS, Ru-ZIS, and Ni-ZIS.

calculated at a plane wave cutoff value of 400 eV. Using the projector-augmented wave (PAW) approach [32,33], ion–electron correlations were described based on pseudopotentials. The Perdew–Burke–Ernzerhof (PBE) functional with generalized gradient approximation (GGA) was used to treat the exchange–correlation functional [34]. The DFT-D3 correction was applied to ensure accurate chemisorption energy by fixing the van der Waals interactions between adsorbate and substrate [35]. We used the Monkhorst–Pack scheme to approximate the Brillouin zone integration [36]. The geometries were optimized until the energy converged to  $5 \times 10^{-5}$  eV/atom and forces were reduced to 0.02 eV/Å [37].

Free energy ( $\Delta G_H^*$ ) was calculated based on the computational hydrogen electrode (CHE) concept, as demonstrated in Eq. (1):

$$\Delta G = \Delta E - T\Delta S + \Delta ZPE - neU, \quad (1)$$

where  $\Delta E$  is the total energy directly computed through the DFT simulations,  $\Delta ZPE$  represents the zero-point energies (ZPE) changes,  $T$  ( $= 298.15$  K) is the room temperature, and  $\Delta S$  is the change in entropy.  $U$  represents the operational electrochemical potential over a conventional hydrogen electrode and  $n$  is the number of electrons transferred during the reaction. The entropy and ZPE of the adsorbed  $H^*$  at the catalyst were extracted from the frequency calculations. For  $ZnIn_2S_4$  (or ZIS), we selected a  $p(3 \times 3)$ –(001) surface for its energy efficiency in the hydrogen evolution reaction (HER) [38]. During structural relaxation, all atoms in our catalytic systems were allowed free to move along the X, Y, and Z directions. To avoid lateral interactions between subsequent images, a 15-Å vacuum region was maintained in the Z-direction [39].

### 3. Results and discussion

#### 3.1. Structural analyses

The phase purity and crystal structure of pristine ZIS, Ni-ZIS, and different Ru-loaded ZIS materials, investigated using XRD spectrometry, are presented in Fig. 1(a). The pristine ZIS showed distinct diffraction planes of (006), (102), (104), (110), and (120), corresponding to  $2\theta$  values of  $21.55^\circ$ ,  $27.27^\circ$ ,  $30.36^\circ$ ,  $47.20^\circ$ , and  $52.46^\circ$ . The evolved miller indices of pristine ZIS represented a hexagonal structure (JCPDS card No. 65–2023) [40]. The XRD patterns of Ni-ZIS and RZ-0.05 to RZ-0.20 were nearly similar to pristine ZIS. In the (006) XRD plane, we observed a small shift in peak amplitudes with increasing Ru concentration, suggesting that the introduction of heteroatoms affected XRD peak intensity [41]. Increased Ru doping influenced the hexagonal structure, as evidenced in sharp crystalline planes in RZ-0.225 to RZ-0.25. RZ-0.25 showed crystalline planes at  $22.32^\circ$ ,  $31.81^\circ$ ,  $35.62^\circ$ ,  $39.16^\circ$ ,  $45.60^\circ$ ,  $47.26^\circ$ , and  $51.35^\circ$ , with representative miller indices at (006), (105), (0010), (108), (0010), (112), (0012), and (203). RZ-0.25 still exhibited a hexagonal structure (JCPDS No. 72–0773); the crystal structure of ZIS exhibits different polytypes depending on the differences in sulfur atom stacking within the matrix [42]. Thus, all the synthesized materials had hexagonal structure and no impurities; the sharp crystalline planes were dependent on Ru doping concentration, which improved crystallinity.

The BET surface area plots of pristine ZIS, Ni-ZIS, and optimized RZ-0.20 photocatalysts, analyzed using Nitrogen adsorption–desorption isotherms, are shown in Fig. 1(b). The plots display type IV isotherms and H3-type hysteresis loops, which reflect the materials' mesoporous nature [43]. The BET surface areas of ZIS, Ni-ZIS, and RZ-0.20 were

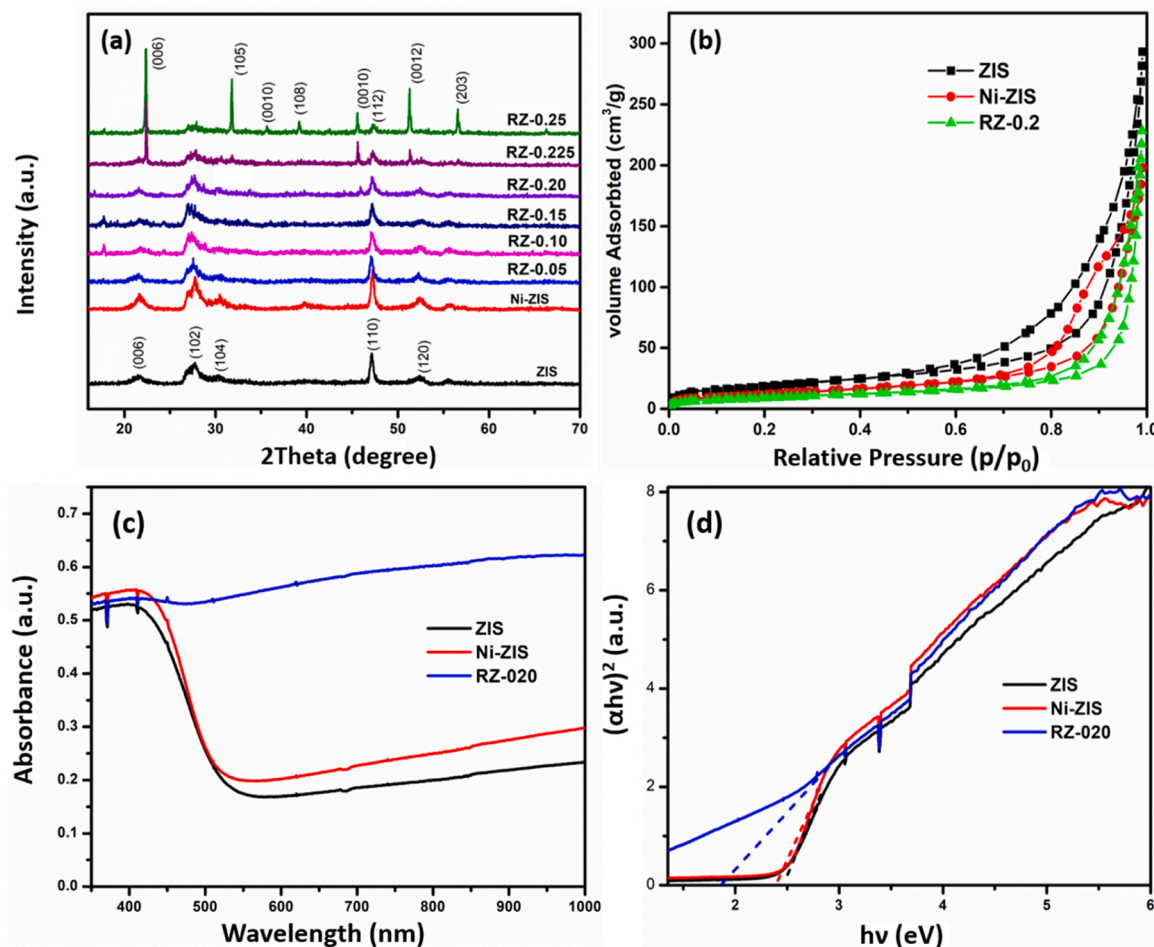


Fig. 1. (a) XRD patterns, (b) BET surface area, (c) DRS UV-Vis spectra, and (d)  $h\nu$  vs.  $(ah\nu)^2$  plots of ZIS, Ni-ZIS, and RZ-0.20.



68.21, 44.97, and 33.52 m<sup>2</sup>/g, respectively. Therefore, pure ZIS nanosheets had greater surface areas than other materials. The lower BET surface areas in Ni/Ru-treated ZIS nanosheets resulted from the ultrathin metal-doped ZIS nanosheets agglomerating under high free surface energies [44,45]. Therefore, the incorporation of heteroatom nanoparticles on ZIS had a strong effect on catalyst surface area. We assumed that the lower surface area of the photocatalysts would not affect visible light absorption during the photo-reaction.

The DRS UV-Vis spectra (Fig. 1(c,d)) showed that ZIS and Ni-ZIS exhibited a broad absorption range in the visible spectrum, with an absorption edge of  $\approx 560$  nm, whereas that of RZ-0.20 extended from the visible to near infrared (NIR) spectra, with a small hump around 500 nm, and further to long-wavelength spectra [46,47]. We evaluated the energy band gap ( $E_g$ ) by plotting the photon energy ( $h\nu$ ) against  $(\alpha h\nu)^2$ , where  $\alpha$  is the absorption coefficient [48]. The estimated tangential  $E_g$  values of ZIS, Ni-ZIS, and RZ-0.20 were 2.41, 2.34, and 1.59 eV, reflecting a decrease with increased metal doping. Corresponding to the changes in optical spectra, the metal atoms may create shallow energy levels next to the ZIS to reduce the  $E_g$  value, which is also consistent with an earlier report [49]. The moderate  $E_g$  value ( $\sim 1.59$  eV) reflects the effective visible light absorption and rapid photo-induced charge separation capacities of Ru-doped ZIN compared with the other materials.

### 3.2. Microstructural characterizations

The FESEM images of pristine ZIS, Ni-ZIS, and Ru-doped materials are shown in Fig. 2(a–f) and S1(a–g). All materials had micro-flower-like structures with distinct petals. The flowers had sizes of a few  $\mu\text{m}$ , with a petals petal width of 12–21 nm. RZ-0.05 and RZ-0.10 showed clear

flower arrangements, reflecting uniform distribution of dopants (Ni or Ru) inside the ZIS lattice. Higher Ru dose resulted in nanoparticle decorations on the micro-flowers (Fig. 2(e)). This indicates that increasing dopant concentrations improved the distribution of ZIS flower nanosheets. FESEM analysis of nanosheet composition showed that RZ-0.20 contained Ru, In, Zn, and S (Fig. 2(g)), with a relatively uniform distribution. EDS analysis of RZ-0.20 (Fig. 2(h)) identified Ru, In, Zn, and S, distributed into their respective atomic ratios without other impurities. In contrast, the micrographs for RZ-0.25 showed agglomerated nanoparticles covering the ZIS micro-flower, leading to a bulk-type morphology, consistent with the elemental mapping analysis (Fig. S1). FESEM analysis showed that the recycled photocatalyst (RZ-0.20) had good stability and maintained structural integrity (Fig. 2(i,j)).

The aberration-corrected high-angle annular dark-field STEM (AC-STEM) analysis of the optimized RZ-0.20 photocatalyst showed a disorderly distribution of thin nanosheets and few nanoparticles (Fig. S2). The vertical and horizontal aligned ZIS nanosheets had interplanar spacing ( $d$ ) values of  $d_{(006)} \approx 0.41$  nm and  $d_{(102)} \approx 0.32$  nm (Fig. S2(b)), which are almost consistent with previous results [50,51]. Fig. 3(a) shows the ultrathin single-layer ZIS nanosheet, and the simulated orange square displays the bright Ru (red circles) sites decorating the ZIS surface (Fig. 3b). Fig. S2(c) displays the horizontal aligned ZIS nanosheets ( $d_{(104)} \approx 0.29$  nm), and the dark-field simulated picture with black (red circle) spots on the ZIS surface (Fig. S2d) likely indicate the Ru nanoparticles. The elemental color mapping analysis indicated a uniform distribution of Ru, Zn, In, and S with no other impurities (Fig. 3(d)). We performed two-line scan profiles of the AC-STEM images at two different positions. Both the first and second line scan profiles (Fig. S3) corresponded to Ru, Zn, In, and S in the single ZIS nanosheet. The intensity of line scan profiles varied based on the atomic concentrations

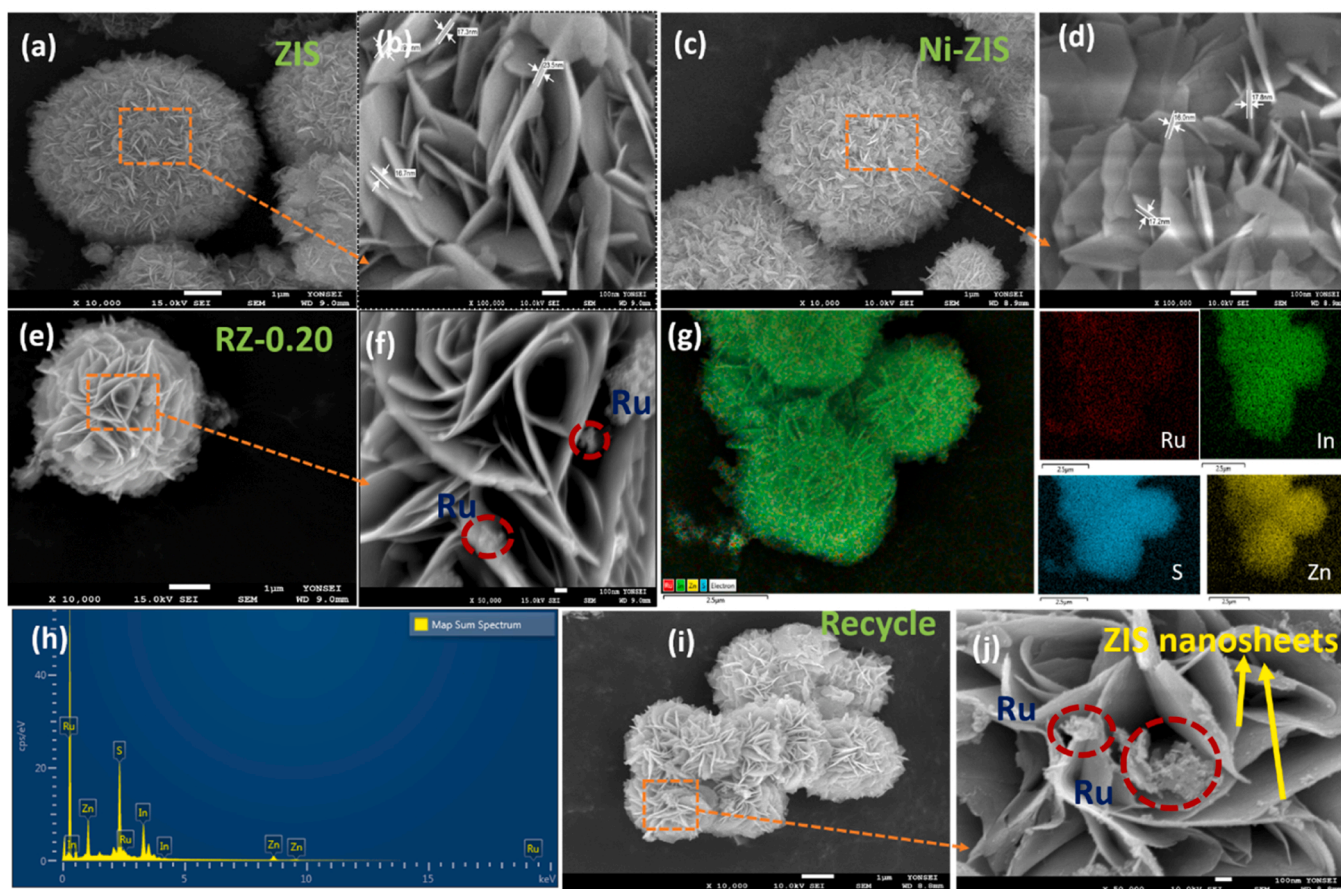


**Fig. 2.** (a–f) FESEM images of pure ZIS, Ni-ZIS, and RZ-0.20; (g) elemental mapping; (h) EDS spectra of RZ-0.20; and (i,j) FESEM of recycled (RZ-0.20) catalyst and its simulated image.



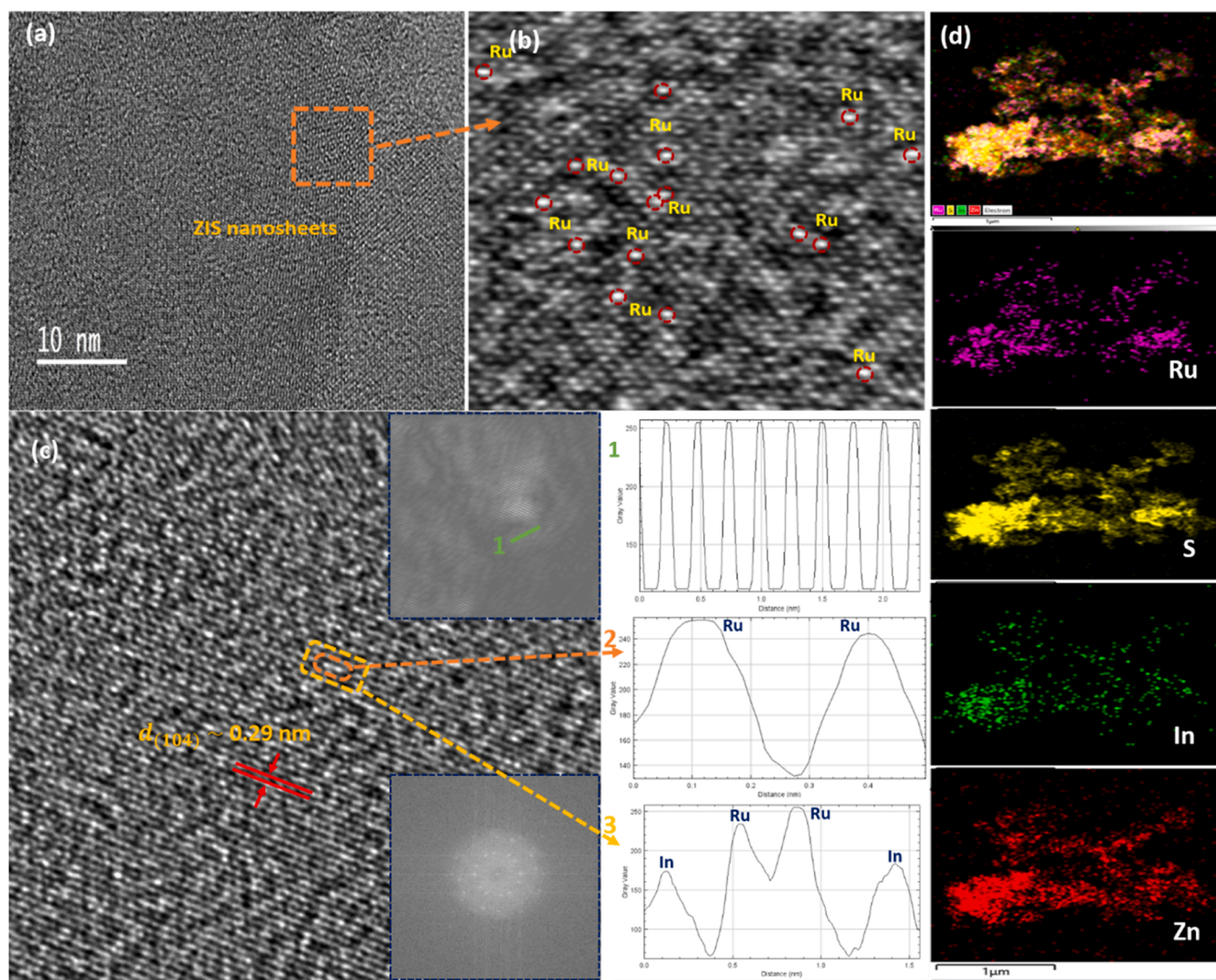


**Fig. 3.** (a) AC-STEM image; (b,c) simulated AC-STEM image of horizontal nanosheets (inserted FFT and IFFT images); green line in (1): IFFT plot profiles, along the line of two spots (orange square) and four bright spots (yellow square). (d) Elemental color mapping of optimized RZ-0.20 photocatalyst.

(Tables S1 and S2). The presence of these elements was confirmed by AC-STEM-based EDS (Fig. S2(e)). High resolution AC-STEM analysis (Fig. 3(c)) identified Fast Fourier transform (FFT) patterns with bright rings, corresponding to a hexagonal crystalline structure, consistent with the crystalline planes of ZIS (Fig. 1(a) and S2(e)). The plot profiles (along the 'green' line in the inverse FFT image labeled with black lines) showed distinct and well distributed profiles ( $d_{(104)} \approx 0.29$  nm). Plot profiles were obtained along the line of two and four bright spots [numbers 2 (orange square) and 3 (yellow square) in Fig. 3(c), respectively]. The two-spot profile had two high-intensity peaks, which we assumed corresponded to Ru sites. The Ru–Ru bond lengths were 0.286 nm (two spots) and 0.311 nm (four spots), which are much higher than the theoretical length (0.232 nm), which reflects the dispersed nature of the Ru atoms [52,53]. Moreover, the four-spot profile revealed that Ru sites aligned between the In sites, which was assigned based on earlier reports [38]. Thus, STEM, elemental mapping, line scan profiles, and EDS characterizations confirmed the Ru nanoparticles in RZ-0.20 were incorporated into the ZIS nanosheet lattice.

XPS analysis of the elemental and chemical states of pristine ZIS and optimized RZ-0.20 XPS (Fig. 4a) identified Zn 2p, In 3d, and S 2p in the pure ZIS and optimized catalyst, with Ru 3d only incorporated in the latter. The full spectrum of RZ-0.20 showed a reduced intensity compared to that of pure ZIS, which is consistent with the XPS spectra of

the respective elements and related to the incorporation of Ru into the ZIS lattice. The high resolution XPS spectra of pristine ZIS showed that Zn 2p was deconvoluted into doublets at 1022.06, with 1045.11 eV corresponding to Zn 2p<sub>3/2</sub> and Zn 2p<sub>1/2</sub>; the binding energy (BE) peaks of In 3d were centered at 445.21 and 452.74 eV, which we designated In 3d<sub>5/2</sub> and In 3d<sub>3/2</sub>, respectively [17,54]. The core-level spectra of S 2p were centered at 161.88 and 163.02 eV in ZIS, and appointed S 2p<sub>3/2</sub> and S 2p<sub>1/2</sub>, respectively. The fine structure of Zn 2p and In 3d shifted by  $\sim 0.2$  eV in RZ-0.20 compared to pure ZIS, reflecting the strong chemical interaction between Ru atoms and the ZIS lattice [55,56]. The Ru–S bond in RZ-0.20 was identified at 161.9 and 168.7 eV; the S 2p BE peaks at 163.1 and 166.9 eV were designated S 2p<sub>3/2</sub> and S 2p<sub>1/2</sub>, respectively [31]. A visible peak shift of  $\sim 0.1$  eV was observed for S 2p, which may be related to the high density electron charge transfer of S(II) to metal species, which reduces shielding of the inner-layer electrons. Consistent with previous findings [57], the deconvolution of Ru 3d into doublets occurred at a BE of 281.0 and 285.0 eV, corresponding to Ru 3d<sub>5/2</sub> and Ru 3d<sub>3/2</sub>, respectively. Further, the appearance of strong Ru–S bonds may indirectly represent the replacement of surface-layer Zn sites by Ru, which further establishes bonds with surrounding S atoms, as indicated by the strong BE peak in S 2p. Collectively, the FESEM, AC-STEM, and XPS analyses all confirm the presence of Ru species in the ZIS nanosheets.

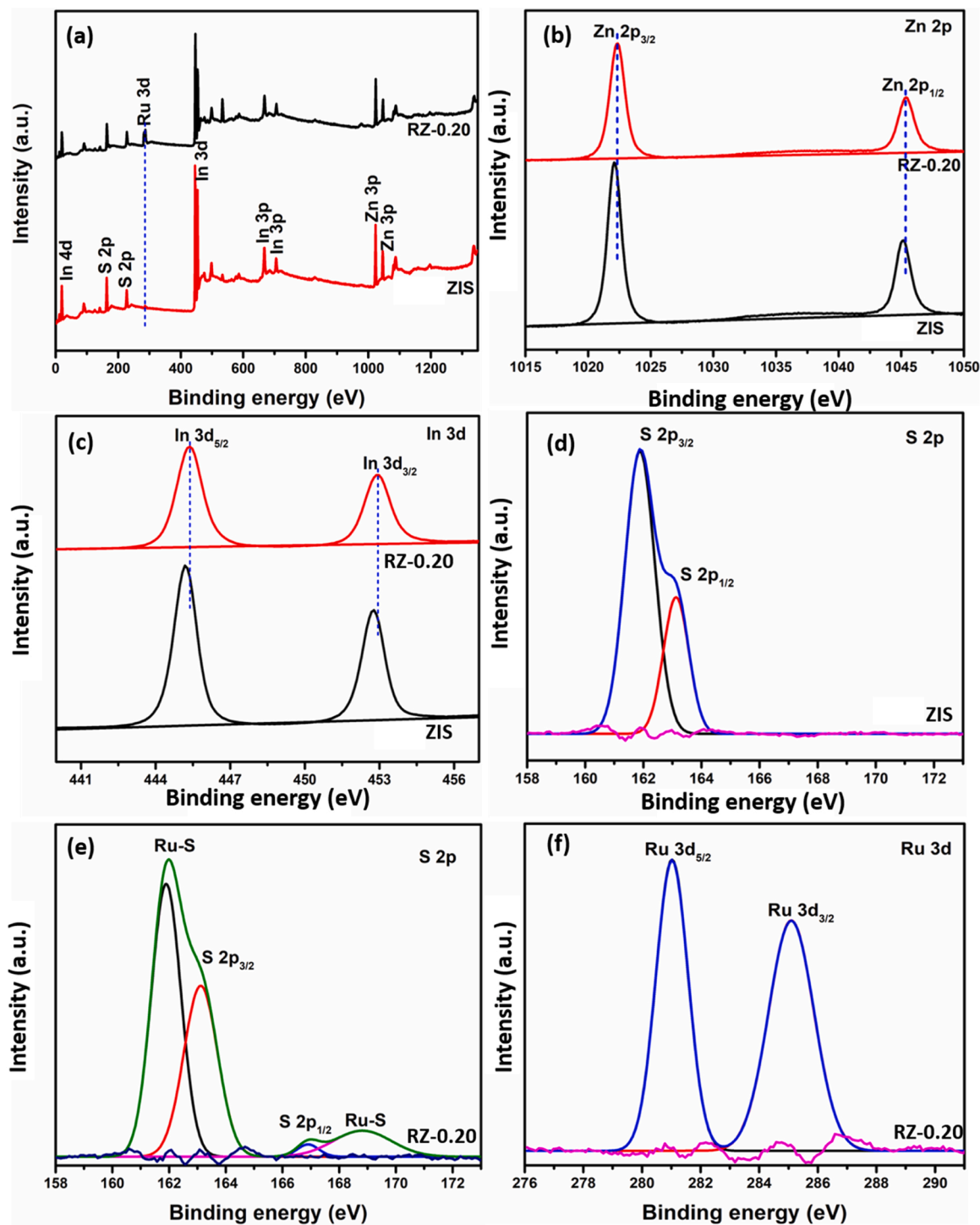


Fig. 4. (a) XPS spectra; high resolution XPS spectra of (b) Zn 2p, (c) In 3d, (d,e) S 2p, and (f) Ru 3d for ZIS and RZ-0.20.

### 3.3. Photocatalytic H<sub>2</sub> evolution performance

We analyzed photocatalytic H<sub>2</sub> evolution in deionized water containing triethanolamine (TEOA) as a scavenger under simulated solar light irradiation. We compared pure ZIS to ZIS containing 0.10 mmol Ni or Ru and found that Ru-ZIS had superior H<sub>2</sub> production rates compared to ZIS (2682.9  $\mu\text{mol} \cdot \text{h}^{-1} \cdot \text{g}^{-1}$ ) and Ni-ZIS (4500  $\mu\text{mol} \cdot \text{h}^{-1} \cdot \text{g}^{-1}$ , Fig. S4). Because the interstitial In and Zn sites are expected to be easily replaced by Ni and Ru, while Ru coordinates the surface-layer Zn–S interactions, a cloud of S ions should be established to enrich electron transfer ability. All Ru-doped ZIS materials showed improved H<sub>2</sub> evolution rates

compared to pristine ZIS. H<sub>2</sub> production rates increased with increasing Ru concentration because of the increasing number of reactive surface sites and improved photo-excited charge separation. The H<sub>2</sub> evolution rate of RZ-0.20 (26 400  $\mu\text{mol} \cdot \text{h}^{-1} \cdot \text{g}^{-1}$ ) was 9.39-fold higher than that of pristine ZIS. Photo-activity decreased at Ru concentrations above 0.225 and 0.25 mmol, which is associated with the reduced visible light absorption ability and spatial charge acceleration between the Ru and ZIS nanosheets under excessive Ru nanoparticle loading, consistent with the FESEM results (Fig. S1) [58]. We evaluated the reproducibility of the optimized RZ-0.20 nanocatalyst in five repeated experiments (Fig. S5) and found consistent photocatalytic water splitting activity between



measurements ( $\sim 26\,400\ \mu\text{mol}\cdot\text{h}^{-1}\cdot\text{g}^{-1}$  under 4 h solar light irradiation), indicating excellent reproducibility.

The photo-stability of the optimized photocatalyst was assessed based on the photocatalytic  $\text{H}_2$  evolution rates in four cycles under 4 h solar light irradiation (Fig. 5(b)). The liquid-dispersed photocatalyst underwent degasification and purging before photo-irradiation to create an inert atmosphere before performing the  $\text{H}_2$  evolution experiment, and the other three cycles were conducted following the same procedure. Following the decreased photo-activity observed in the fifth cycle, it was hypothesized that oxidation of the scavenger might be the cause. To address this, an additional 3 mL of TEOA was introduced into the reactor, and subsequent cycling measurements were carried out using a procedure similar to previous experiments. Interestingly, the results displayed nearly identical photo-activity compared to the first cycle. The long-term stability experiment showed that the photo-activity gradually increased over 12 h of light irradiation to  $316\,795\ \mu\text{mol}\cdot\text{g}^{-1}$ , where it was maintained for most of the reaction (Fig. 5(c)). Compared to pure ZIS and Ni-ZIS, the optimized catalyst showed an enhanced  $\text{H}_2$  evolution performance. To confirm the stability of the optimized catalyst, we thoroughly washed and dried the used catalyst after 4 h of light irradiation before each successive analysis. Microstructural analysis by FESEM (Fig. 2(i,j)) indicated a decorated micro-flower-type morphology similar to that of unused RZ-0.20. Recycling and long-term stability experiments confirmed the strong stability and durability of the optimized RZ-0.20 photocatalyst. We assessed the effects of various scavengers on the optimized catalyst (Fig. 5(d)). As sacrificial reagents, we used ethanol as neutral solvent, LA as acidic reagent, TEOA as basic reagent, and  $\text{Na}_2\text{S}/\text{Na}_2\text{SO}_3$  as alkaline solution. The 3-mL TEOA treatment promoted  $\text{H}_2$  evolution rates to a greater extent than the other treatments.

### 3.4. Photoluminescence (PL), time resolved-PL, photoelectrochemical (PEC), and Mott–Schottky measurements

The efficient separation of photo-induced charges and charge dynamic behavior for sub-sequential rapid  $\text{H}_2$  evolution in the synthesized nanomaterials were investigated using PL and PEC measurements. The PL spectra showed lower intensities with Ru doping than those for pristine ZIS and Ni-ZIS (Fig. 6a), confirming increased charge separation with Ru doping. To elucidate the electron migration mechanism in ZIS, Ni-ZIS, and RZ-0.20, we analyzed the charge carrier kinetics of the photocatalysts using time-resolved fluorescence decay spectroscopy (TRPL, Fig. 6b), and calculated the average fluorescence lifetime ( $\tau_A$ ) as follows [59]:

$$\tau_A = \frac{A_1\tau_1^2 + A_2\tau_2^2}{A_1\tau_1 + A_2\tau_2} \quad (2)$$

where  $A_1$  and  $A_2$  are amplitudes,  $\tau_1$  indicates nonradioactive recombination of charge carriers in the defect states of ZIS, and  $\tau_2$  reflects the recombination of free electron–hole pairs [60]. The average lifetime of RZ-0.20 was 0.057 ns, which is shorter than that for Ni-ZIS (0.543 ns) and pristine ZIS (0.075 ns). Notably, the photo-excited electrons on the optimized catalyst could rapidly transfer from ZIS nanosheets to surface Ru reactive sites to promote surface photo-reactions. The PL and TR-PL results of charge carrier migration kinetics showed that the synergetic interaction of the ZIS nanosheets and Ru sites greatly promoted charge separation, consistent with the increase in photocatalytic  $\text{H}_2$  evolution rates.

Under solar irradiation with on/off cycles (Fig. 6(c)), RZ-0.20 displayed the highest photocurrent compared to pristine and Ni-doped ZIS [46], indicating that RZ-0.20 has greater electron separation and -acceleration abilities. The Nyquist plots (Fig. 6d and S6) of pristine ZIS, Ni-ZIS, RZ-0.20, and RZ-0.25 nanomaterials revealed that the optimized

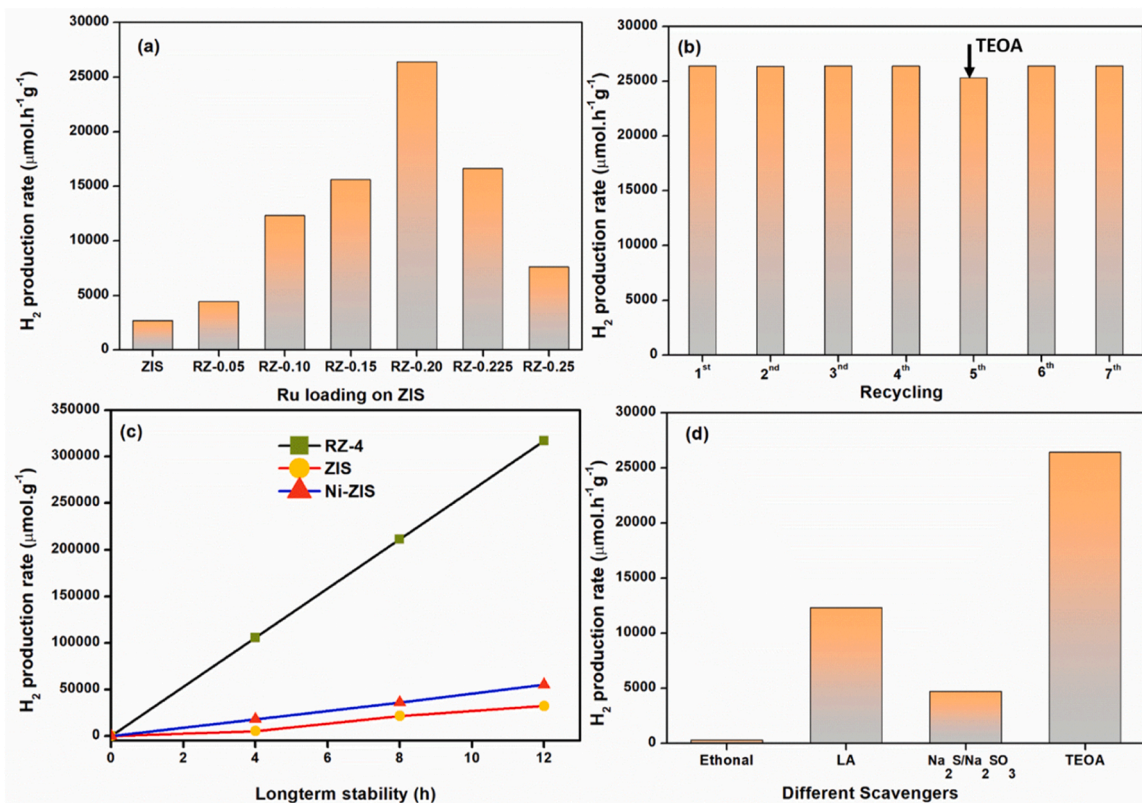


Fig. 5. (a) Photocatalytic  $\text{H}_2$  production rates in pristine ZIS and Ru-ZIS with different Ru contents; (b) recycling experiments; (c) long-term stability experiment and photo-activity comparison between various scavengers in the optimized RZ-0.20 photocatalyst.



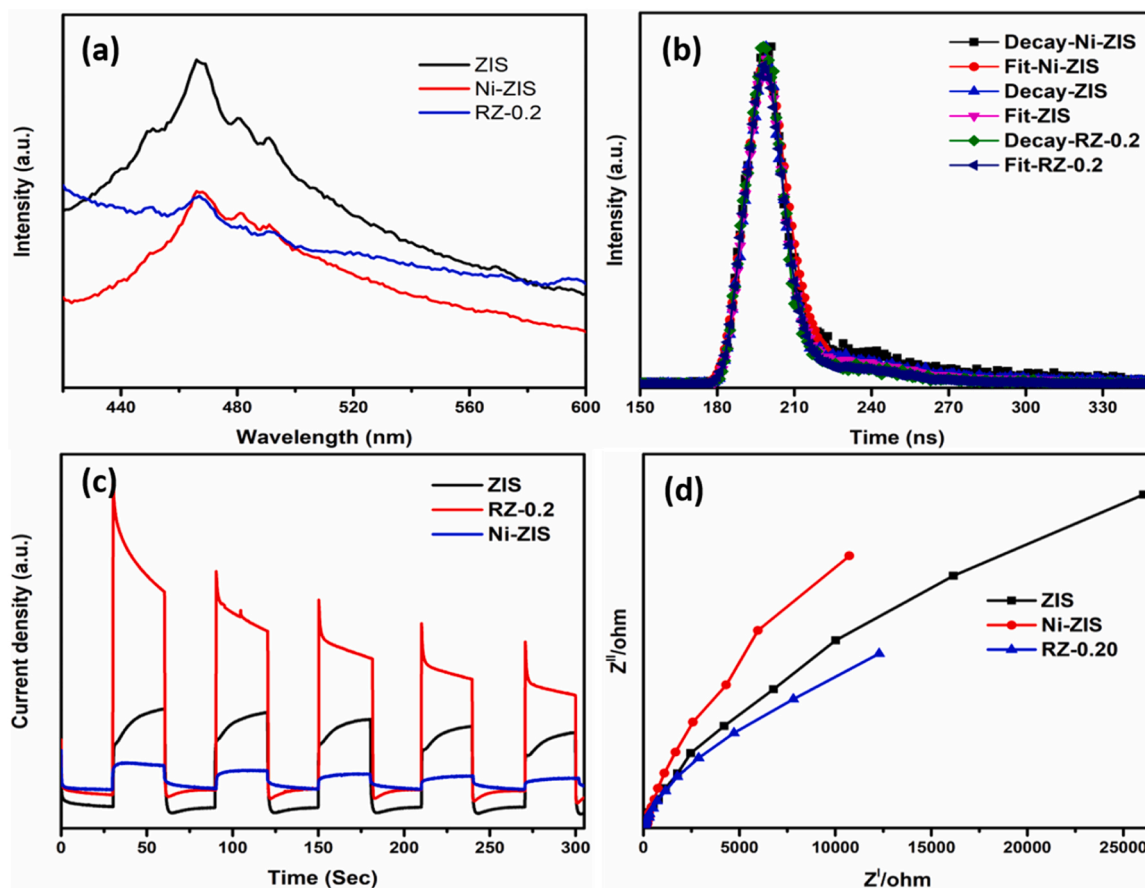


Fig. 6. (a) PL spectra, (b) time resolved-PL spectra, (c) photocurrent cycles, and (d) impedance spectra of pristine ZIS, Ni-ZIS, and RZ-0.20.

catalysts showed smaller orca radii than the other materials, likely because the optimized catalysts have less surface defects and imperfections [61] and fewer charge migration barriers for effective photo-induced electron acceleration and charge pair separation [62]. RZ-0.25 had a comparatively high orca radius, reflecting the increase in crystal defects and surface aggregations with increasing dopant concentration [63], consistent with the FESEM results. PEC measurements confirmed that the optimized catalyst efficiently promoted  $\text{H}_2$  evolution by increasing the number of surface reactive sites on the ultrathin 2D ZIS nanosheet and promoting rapid  $\text{H}^+$  intermediate absorption and desorption.

We further assessed the photo-induced electron-hole pair separation and charge kinetics underlying the photocatalytic reaction mechanism of  $\text{H}_2$  evolution based on the band edge potentials of the photocatalysts. The electrochemical Mott-Schottky (MS) plots were analyzed to estimate the energy levels of the conduction band (CB) edge potentials. The flat band potentials of pristine ZIS, Ni-ZIS, and RZ-0.20 were  $-1.01$ ,  $-0.922$ , and  $-0.913$  V vs.  $\text{E}_{\text{Ag}/\text{AgCl}}$ , respectively (Fig. S7). The CB edge potential of the n-type semiconductor was  $0.1$  eV lower than the flat band potentials [64,65]. We added the calculated potentials vs.  $\text{E}_{\text{Ag}/\text{AgCl}}$  to the normal hydrogen electrode (NHE) scale using  $E_{\text{NHE}} = E_{\text{Ag}/\text{AgCl}} + 0.197$  [66] and found that the evaluated CB ( $E_{\text{CB}}$ ) potentials were  $-0.71$ ,  $-0.625$ , and  $-0.616$  V vs. NHE for pristine ZIS, Ni-ZIS, and RZ-0.20, respectively. The edge potentials were high for all the synthesized material compared to the reduction potential of  $\text{H}^+$ , indicating that the photocatalysts were appropriate for water dissociation. The valence band (VB) potentials ( $E_{\text{VB}}$ ) were  $1.74$ ,  $1.80$ , and  $1.18$  V based on the optical energy band gap and CB values for pristine ZIS, Ni-ZIS, and RZ-0.20, respectively [67], [68]. The RZ-0.20 nanomaterial had lower CB potentials than pristine ZIS and Ni-ZIS, reflecting the strong interaction between Ru and ZIS along with the shallow energy states induced

by the dopant, which efficiently reduced the charge migration barrier and promoted charge transfer to reactive surface sites, where the electrons promote water dissociation and enhance  $\text{H}_2$  production.

### 3.5. Plausible photocatalytic mechanism

We propose a plausible photocatalytic reaction mechanism for Ru-ZIS based on the photocatalytic performance and PEC results (Fig. 7). Initially, the electron-hole pairs effectively separated in ZIS nanosheets under solar light irradiation, the photo-generated conduction electrons of ZIS migrated to the shallow energy states of Ru active sites through

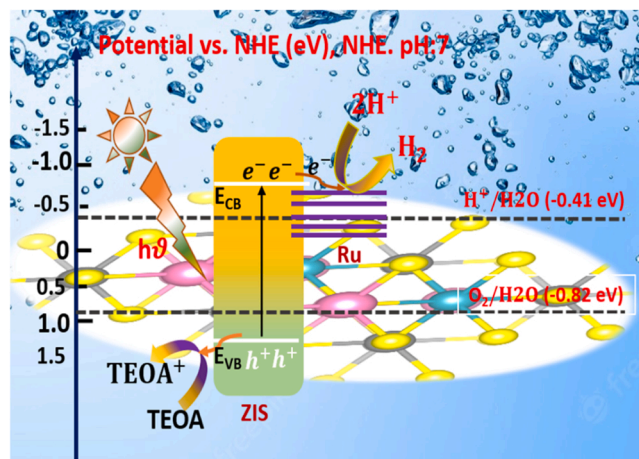


Fig. 7. Plausible photocatalytic reaction mechanism of Ru-ZIS under simulated solar irradiation.

the Schottky junctions arising between ZIS and Ru nanoparticles. The Schottky barrier effectively inhibited the backward flow of conduction electrons, promoting the separation of electrons and holes [69]. Thereafter, electron–hole charge-pair recombination decreased greatly owing to the unavailability of adjacent holes for recombination in the VB of ZIS. A strong electronic cloud accumulated at the shallow energy levels of Ru, consistent with the TRPL results indicate reduced  $\tau_A$  values. Here, the surface shuttled electrons participate in water dissociation to enhance  $H_2$  evolution. The VB potentials (based on optical band gap and Mott–Schottky values) suggested that the holes in ZIS reacted with the TEOA hole supplier, suggesting that TEOA was oxidized into its oxidation product. This effectively hampered charge pair recombination in the Ru-ZIS Schottky junction.

This simple and single-component optimized RZ-0.20 photocatalyst exhibited superior  $H_2$  evolution performance, largely due to the one-directional charge migration behavior of the 2D ultrathin ZIS nanosheets and increase in reactive sites with Ru incorporation. Ru sites may replace Zn sites in the ZIS lattice and bond with surrounding S atoms in high-electron-density clouds (due to the high number of electrons participating in the Ru–S bond). The Ru reactive sites provided shallow energy levels, effectively reducing the charge migration length via the Schottky barrier. These characteristics enhanced the visible light absorption, charge separation, and electron kinetic capacities of the Ru-ZIS, while the accumulation of electrons promote water splitting for  $H_2$  production. The optimized catalyst showed improved performance over previous catalysts (Table S3).

We performed periodic density functional theory simulations to elucidate the HER activity of the metal-doped ZIS nanosheets. HER kinetics can be improved by (i) substitutional or (ii) interstitial doping. Here, we adopted the substitutional doping technique with the incorporation of Ru and Ni atoms. We determined the most stable position for dopant atoms based on four combinations with the Zn and In sites [(i) Ni at the Zn site, (ii) Ni at the In site, (iii) Ru at the Zn site, and (iv) Ru at the In site] at the ZIS. The Ni and Ru dopants were most stable at the In (sub-layer) and Zn (top-layer) sites of ZIS, respectively. Note that the total energies of (i) Ni at the In site and (ii) Ru at the Zn site were 0.77 eV (Ni) and 0.85 eV (Ru) lower than those of (iii) Ni at the Zn site and (iv) Ru at the In site, respectively. This indicates that the photocatalysts are thermodynamically stable.

We assessed the influence of Ru and Ni doping on the HER activity of the ZIS catalyst (Fig. S8) based on the  $H^*$  adsorption energy at interacting surface S sites. Our DFT calculation predicted a reduction in  $H^*$  affinity with the incorporation of Ru or Ni compared to that for pure ZIS. The  $H^*$  adsorption energy ( $E_{ad}$ ) for ZIS, Ni-doped ZIS, and Ru-doped ZIS was  $-3.43$  eV,  $-3.47$  eV, and  $-2.22$  eV, respectively (see Fig. 8a–c for H configuration).

We investigated the HER free energy profiles of the ZIS, Ni-ZIS, and Ru-ZIS catalysts (Fig. 8d–f) based on the Volmer–Heyrovský mechanism:

- (1)  $H^+(aq) + e^- \rightarrow H^*$  (Volmer step)
- (2)  $H^* + H^+(aq) + e^- \rightarrow H_2(g)$  (Heyrovský step).

The HER onset potential ( $U$ ) of Ru-ZIS was  $-0.05$  V, significantly lower than that for ZIS ( $-1.17$  V) and Ni-ZIS ( $-1.20$  V), reflecting the greatly enhanced HER activity associated with Ru doping. This is closely related to the reduction in  $H^*$  affinity in the presence of Ru on the surface layer. Consistent with our experimental observations, Ru-ZIS showed weaker binding affinity for  $H^*$  species ( $E_{bin} = -2.22$  eV) than ZIS ( $E_{bin} = -3.44$  eV) and Ni-ZIS ( $E_{bin} = -3.47$  eV), which suggests that the energy required for the (2)  $H^+(aq) + e^- + H^* \rightarrow H_2(g)$  step is significantly lowered under neutral conditions ( $pH = 0$ ). HER activity is known to improve with the proximity of  $G_{H^*}$  to the thermoneutral level ( $\Delta G_{H^*} \approx 0$ ). The Gibbs free energy was near zero when incorporating the Ru atom in the ZIS catalyst, suggesting that Ru doping boosted HER kinetics and  $H^*$  desorption. A recent study on Pt-ZIS showed that single protruding Pt atoms could prevent electron–hole pair coupling and produce a tip effect, which promotes the adsorption/desorption of  $H^*$  through efficient proton mass transfer and enhances the HER thermodynamics and kinetics [38].

We performed a projected density of states (PDOS) analysis to elucidate the catalytic performance and orbital overlaps between the adsorbed  $H^*$  and pure, Ni-, and Ru-doped ZIS. Different orbitals existed in our catalytic systems, including Zn-3d, In-5 s, S-2p, Ni-3d, and Ru-4d. The In-5p orbital strongly hybridized with the S-2p orbital in the CBM region (Fig. 9(a–c)), reflecting the strong chemical bond between the In and S atoms. In addition, the Zn-3d states strongly overlapped with S-2p from  $-0.2$  eV to  $2.1$  eV, reflecting the strong Zn–S bonding. The 1 s orbital of  $H^*$  were strongly hybridized with the S-2p orbital in the VB

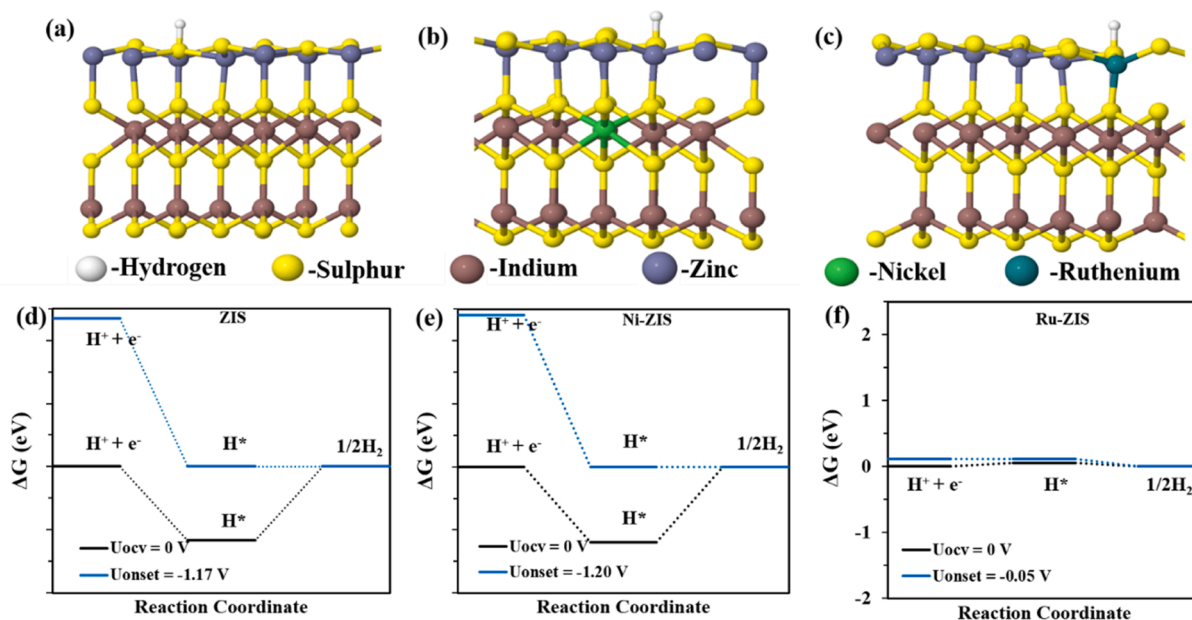


**Fig. 8.** (a–c) Computed structures of H in (a) ZIS, (b) Ni-ZIS, and (c) Ru-ZIS. The yellow, dark blue, brown, green, dark green, and white spheres indicate sulfur, zinc, indium, nickel, ruthenium, and hydrogen atoms, respectively. Computed free energy of  $H^*$  adsorption in (d) pure ZIS, (e) Ni-ZIS, and (f) Ru-ZIS respectively.

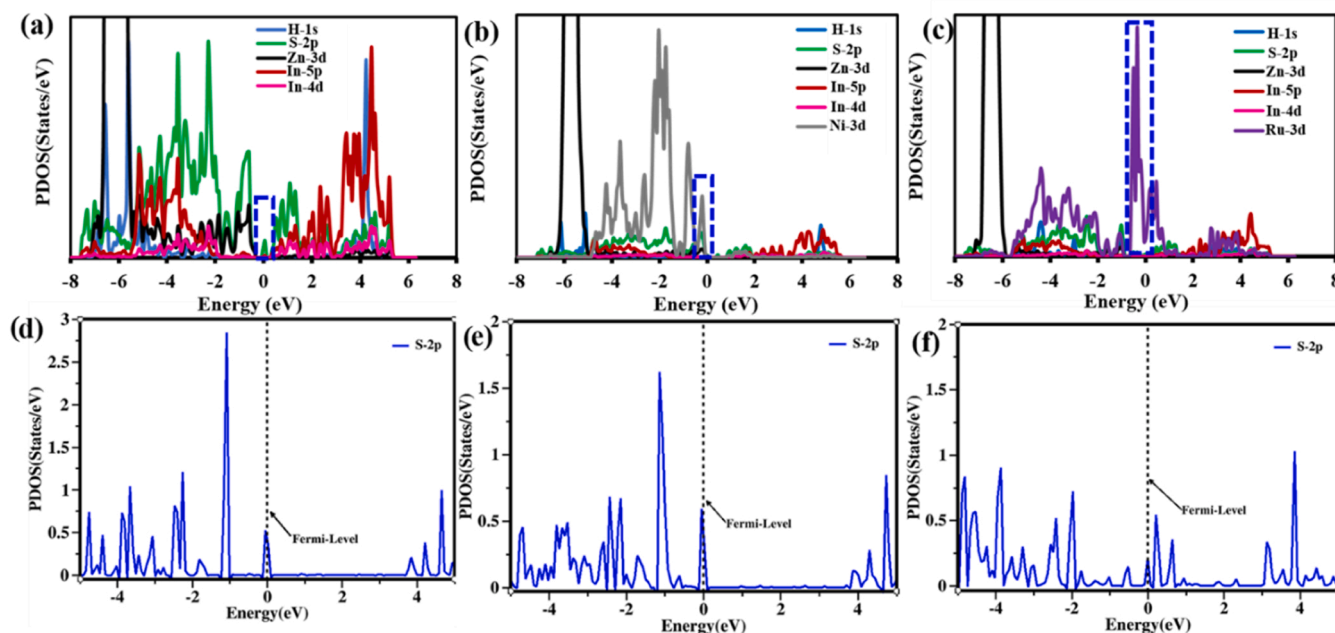


**Fig. 9.** PDOS plots of (a) pure, (b) Ni-ZIS, and (c) Ru-ZIS. PDOS plots of the S-2p orbital in H-adsorbed (d) pure ZIS, (e) Ni-ZIS, and (f) Ru-ZIS; 0 eV indicates the Fermi level.

region from  $-5.4$  eV to  $-6.5$  eV, confirming the adsorbed state of  $H^*$  in pure ZIS and Ni-ZIS. In contrast, the  $1s$  of  $H^*$  hybridized strongly with S-2p from  $-4.1$  eV to  $5.8$  eV in Ru-ZIS. The In-2p orbital strongly overlapped with the S-2p orbital in the VB region of Ni- and Ru-ZIS, confirming strong In-S bonding. In addition, the Ni-3d and Ru-4d orbitals in Ni- and Ru-doped ZIS catalysts were strongly hybridized with the S-2p orbitals throughout the VBM region. Carrier concentrations near the Fermi level can strongly influence the catalytic properties of the system. For ZIS, only the S-2p orbital occurred near the Fermi level (Fig. 9d, e); however, 3d-orbital enhanced states appeared near the Fermi level in Ni- and Ru-doped ZIS (Fig. 9f). This suggests that the 3d orbitals may influence the catalytic properties of the ZIS-material. Interestingly, the Ru-doped system enhanced the density of states near  $E_f$  compared to pristine ZIS and Ni-ZIS, corresponding with enhanced catalytic activity and HER performance.

We further investigated the catalytic behavior of the reactive surface site based on the PDOS for selected S-2p atoms in H-adsorbed pure, Ni-doped, and Ru-ZIS (Fig. 9). We found that the PDOS states were significantly reduced near the Fermi level in Ru-ZIS compared to pure and Ni-doped ZIS, suggesting a weakening of the H-S(ZIS) bond in Ru-ZIS, leading to enhanced HER activity, consistent with our experimental results.

#### 4. Conclusions

We investigated the influence of preferential heteroatom substitution in ZIS nanosheets on catalyst photo-activity. The heteroatom substitution replaces Zn/In in the ZIS lattice owing to electrochemical interactions with the dopants. Our study presents a theoretical one-step framework (and mainly hydrothermal treatments) for heteroatom (Ru/Ni)-doped ZIS nanosheet production. We assessed the photocatalytic  $H_2$  production rates over 4 h of solar light irradiation and found that the optimized RZ-0.20 exhibited superior performance ( $26\,400\,\mu\text{mol}\cdot\text{h}^{-1}\cdot\text{g}^{-1}$ ) over pristine ZIS and Ni-ZIS. This enhancement was mainly attributed to the one-dimensional charge transfer ability of ZIS nanosheets and increase in reactive site prevalence with Ru incorporation. Ru was rapidly bonded to the surrounding S atoms, especially because of the strong electron density established by S ions around Ru sites. The

electron cloud at the reactive sites actively promoted water dissociation for superior photocatalytic  $H_2$  evolution. In contrast, less Ni atoms may replace the sub layer of In sites; because the bond in  $[\text{InS}]_6$  requires high energy, Ni bonds with less S sites in the ZIS lattice, supplying few electrons to reactive sites, thus resulting in lower photo-activity. This was further confirmed based on first-principles calculations: Gibbs free was near zero when incorporating Ru into the ZIS catalyst, implying that Ru doping enhanced HER kinetics and H desorption. Interestingly, Ru doping reduced the  $E_{\text{bin}}$  and on-set  $H^*$  potential values, suggesting that less energy is required for the  $(2) H^+(aq) + e^- + H^* \rightarrow H_2(g)$  step under neutral conditions ( $\text{pH} = 0$ ). Therefore, the proposed single-component photocatalyst with one-step synthesis effectively enhanced photo-activity across the Schottky barrier. Our study findings elaborate greatly on the effects of different preferential heteroatom substitution strategies and can inform further research and development in the photocatalytic fields.

#### CRediT authorship contribution statement

**Palagiri Bhavani:** Writing – original draft, Investigation, Conceptualization. **Young-Kwon Park:** Writing – review & editing, Supervision, Conceptualization. **Hyung Chul Ham:** Writing – review & editing, Supervision, Conceptualization. **D. Praveen Kumar:** Investigation, Conceptualization. **Shanmugasundaram Kamalakannan:** Formal analysis, Data curation. **WOYUL KIM:** Writing – review & editing, Supervision, Conceptualization.

#### Declaration of Competing Interest

The authors declare that they have no known competing financial interests or personal relationships that could have appeared to influence the work reported in this paper.

#### Data availability

Data will be made available on request.



## Acknowledgments

This work was supported by the National Research Foundation of Korea (NRF) grant funded by the Korea government (MSIT) (No. NRF-2022M3A9F3017700, NRF-2021R1A5A1084921, and NRF-2021R1I1A1A01057971) and the Korea Evaluation Institute of Industrial Technology (Alchemist Project 20018904, NTIS-141518011) through the Ministry of Trade, Industry and Energy, Korea.

## Appendix A. Supporting information

Supplementary data associated with this article can be found in the online version at [doi:10.1016/j.apcatb.2024.124154](https://doi.org/10.1016/j.apcatb.2024.124154).

## References

- [1] T. Takata, J. Jiang, Y. Sakata, M. Nakabayashi, N. Shibata, V. Nandal, K. Seki, T. Hisatomi, K. Domen, Photocatalytic water splitting with a quantum efficiency of almost unity, *Nature* 581 (2020) 411–414, <https://doi.org/10.1038/s41586-020-2278-9>.
- [2] M. Altomare, N.T. Nguyen, S. Hejazi, P. Schmuki, A COcatalytic Electron-transfer Cascade Site-selectively Placed on TiO<sub>2</sub> nanotubes yields enhanced photocatalytic H<sub>2</sub> evolution, *Adv. Funct. Mater.* 28 (2018) 1704259, <https://doi.org/10.1002/adfm.201704259>.
- [3] M.-L. Xu, M. Lu, G.-Y. Qin, X.-M. Wu, T. Yu, L.-N. Zhang, K. Li, X. Cheng, Y.-Q. Lan, Piezo-photocatalytic synergy in BiFeO<sub>3</sub>@COF Z-scheme heterostructures for high-efficiency overall water splitting, *Angew. Chem. Int. Ed.* 61 (2022) e202210700, <https://doi.org/10.1002/ange.202210700>.
- [4] X. Wei, J. Zhang, L. Wang, Y. Bai, J. Huang, H. She, Q. Wang, Super-hydrophilic BiVO<sub>4</sub>/MgO/FeCo<sub>2</sub>O<sub>4</sub> charge migration achieves efficient photoelectrochemical performance, *Chem. Eng. J.* 482 (2024) 149114, <https://doi.org/10.1016/j.cej.2024.149114>.
- [5] J. Hu, C. Chen, Y. Zheng, G. Zhang, C. Guo, C.M. Li, Spatially separating redox centers on Z-Scheme ZnIn<sub>2</sub>S<sub>4</sub>/BiVO<sub>4</sub> hierarchical heterostructure for highly efficient photocatalytic hydrogen evolution, *Small* 16 (2020) 2002988, <https://doi.org/10.1002/smll.202002988>.
- [6] Y. Yang, Z. Chen, H. Huang, Y. Liu, J. Zou, S. Shen, J. Yan, J. Zhang, Z. Zhuang, Z. Luo, C. Yang, Y. Yu, Z. Zou, Synergistic surface activation during photocatalysis on perovskite derivative sites in heterojunction, *Appl. Catal. B Environ.* 323 (2023) 122146, <https://doi.org/10.1016/j.apcatb.2022.122146>.
- [7] L. Wang, J. Zhang, Y. Li, Y. Shi, J. Huang, Q. Mei, L. Wang, F. Ding, B. Bai, Q. Wang, Heterostructured CoFe<sub>1.5</sub>Cr<sub>0.5</sub>S<sub>3</sub>O/COFs/BiVO<sub>4</sub> photoanode boosts charge extraction for efficient photoelectrochemical water splitting, *Appl. Catal. B Environ.* 336 (2023), <https://doi.org/10.1016/j.apcatb.2023.122921>.
- [8] C. Cui, X. Zhao, X. Su, N. Xi, X. Wang, X. Yu, X.L. Zhang, H. Liu, Y. Sang, Porphyrin-based Donor-Acceptor Covalent Organic Polymer/ZnIn<sub>2</sub>S<sub>4</sub> Z-Scheme Heterostructure for Efficient Photocatalytic Hydrogen Evolution, *Adv. Funct. Mater.* n/a (n.d.) 2208962, <https://doi.org/10.1002/adfm.202208962>.
- [9] X. Wang, X. Wang, J. Huang, S. Li, A. Meng, Z. Li, Interfacial chemical bond and internal electric field modulated Z-scheme Sv-ZnIn<sub>2</sub>S<sub>4</sub>/MoSe<sub>2</sub> photocatalyst for efficient hydrogen evolution, *Nat. Commun.* 12 (2021) 4112, <https://doi.org/10.1038/s41467-021-24511-z>.
- [10] X. Gou, F. Cheng, Y. Shi, L. Zhang, S. Peng, J. Chen, P. Shen, Shape-controlled synthesis of ternary chalcogenide ZnIn<sub>2</sub>S<sub>4</sub> and CuIn(S,Se)<sub>2</sub> nano-/microstructures via facile solution route, *J. Am. Chem. Soc.* 128 (2006) 7222–7229, <https://doi.org/10.1021/ja0580845>.
- [11] Y. Pan, X. Yuan, L. Jiang, H. Yu, J. Zhang, H. Wang, R. Guan, G. Zeng, Recent advances in synthesis, modification and photocatalytic applications of micro/nano-structured zinc indium sulfide, *Chem. Eng. J.* 354 (2018) 407–431, <https://doi.org/10.1016/j.cej.2018.08.028>.
- [12] T. Goswami, D.K. Yadav, H. Bhatt, G. Kaur, A. Shukla, K.J. Babu, H.N. Ghosh, Defect-mediated slow carrier recombination and broad photoluminescence in non-metal-doped ZnIn<sub>2</sub>S<sub>4</sub> nanosheets for enhanced photocatalytic activity, *J. Phys. Chem. Lett.* 12 (2021) 5000–5008, <https://doi.org/10.1021/acs.jpclett.1c01203>.
- [13] W.L. Jia, W.J. Li, H.Y. Yuan, X. Wu, Y. Liu, S. Dai, Q. Cheng, P.F. Liu, H.G. Yang, Surface Cu<sup>+</sup> modified ZnIn<sub>2</sub>S<sub>4</sub> for promoted visible-light photocatalytic hydrogen evolution, *J. Energy Chem.* 74 (2022) 341–348, <https://doi.org/10.1016/j.jechem.2022.07.022>.
- [14] Y. Zhou, Q. Zhang, X. Shi, Q. Song, C. Zhou, D. Jiang, Photocatalytic reduction of CO<sub>2</sub> into CH<sub>4</sub> over Ru-doped TiO<sub>2</sub>: synergy of Ru and oxygen vacancies, *J. Colloid Interface Sci.* 608 (2022) 2809–2819, <https://doi.org/10.1016/j.jcis.2021.11.011>.
- [15] X. Chen, S. Guan, J. Zhou, H. Shang, J. Zhang, F. Lv, H. Yu, H. Li, Z. Bian, Photocatalytic free radical-controlled synthesis of high-performance single-atom catalysts, *Angew. Chem. - Int. Ed.* 62 (2023) 1–9, <https://doi.org/10.1002/ange.202312734>.
- [16] J. Cao, Z. Xu, Y. Chen, S. Li, Y. Jiang, L. Bai, H. Yu, H. Li, Z. Bian, Tailoring the asymmetric structure of NH<sub>2</sub>-UiO-66 metal-organic frameworks for light-promoted selective and efficient gold extraction and separation, *Angew. Chem.* 135 (2023), <https://doi.org/10.1002/ange.202302202>.
- [17] H. Jing, G. Xu, B. Yao, J. Ren, Y. Wang, Z. Fang, Q. Liang, R. Wu, S. Wei, Sulfur vacancy-enriched rhombohedral ZnIn<sub>2</sub>S<sub>4</sub> nanosheets for highly efficient photocatalytic overall water splitting under visible light irradiation, *ACS Appl. Energy Mater.* 5 (2022) 10187–10195, <https://doi.org/10.1021/acsam.2c01930>.
- [18] D. Jing, M. Liu, L. Guo, Enhanced hydrogen production from water over Ni doped ZnIn<sub>2</sub>S<sub>4</sub> microsphere photocatalysts, *Catal. Lett.* 140 (2010) 167–171, <https://doi.org/10.1007/s10562-010-0442-9>.
- [19] Z. Xie, J. Chen, Y. Chen, T. Wang, X. Jiang, Y. Xie, C.-Z. Lu, A Z-scheme Pd modified ZnIn<sub>2</sub>S<sub>4</sub>/P25 heterojunction for enhanced photocatalytic hydrogen evolution, *Appl. Surf. Sci.* 579 (2022) 152003, <https://doi.org/10.1016/j.apsusc.2021.152003>.
- [20] C. Feng, X. Yang, Z. Sun, J. Xue, L. Sun, J. Wang, Z. He, J. Yu, Dual interfacial synergism in Au-Pd/ZnIn<sub>2</sub>S<sub>4</sub> for promoting photocatalytic selective oxidation of aromatic alcohol, *Appl. Surf. Sci.* 501 (2020) 144018, <https://doi.org/10.1016/j.apsusc.2019.144018>.
- [21] M. Ismael, Highly effective ruthenium-doped TiO<sub>2</sub> nanoparticles photocatalyst for visible-light-driven photocatalytic hydrogen production, *N. J. Chem.* 43 (2019) 9596–9605, <https://doi.org/10.1039/C9NJ02226K>.
- [22] Q. Yang, T. Wang, Z. Zheng, B. Xing, C. Li, B. Li, Constructing interfacial active sites in Ru/g-C<sub>3</sub>N<sub>4-x</sub> photocatalyst for boosting H<sub>2</sub> evolution coupled with selective benzyl-alcohol oxidation, *Appl. Catal. B Environ.* 315 (2022) 121575, <https://doi.org/10.1016/j.apcatb.2022.121575>.
- [23] R. Janani, G.S. Priyanga, S. Behara, A.A. Melvin, A.R.M. Shaheer, T. Thomas, B. Neppolian, S. Singh, Enhanced solar light driven hydrogen generation and environment remediation through Nd incorporated ZnIn<sub>2</sub>S<sub>4</sub>, *Renew. Energy* 162 (2020) 2031–2040, <https://doi.org/10.1016/j.renene.2020.09.081>.
- [24] B. Sun, J. Bu, X. Chen, D. Fan, S. Li, Z. Li, W. Zhou, Y. Du, In-situ interstitial zinc doping-mediated efficient charge separation for ZnIn<sub>2</sub>S<sub>4</sub> nanosheets visible-light photocatalysts towards optimized overall water splitting, *Chem. Eng. J.* 435 (2022) 135074, <https://doi.org/10.1016/j.cej.2022.135074>.
- [25] J. Cao, Z. Xu, Y. Chen, S. Li, Y. Jiang, L. Bai, H. Yu, H. Li, Z. Bian, Tailoring the asymmetric structure of NH(2)-UiO-66 metal-organic frameworks for light-promoted selective and efficient gold extraction and separation, *Angew. Chem. Int. Ed. Engl.* 62 (2023) e202302202, <https://doi.org/10.1002/ange.202302202>.
- [26] Y. Chen, S. Guan, H. Ge, X. Chen, Z. Xu, Y. Yue, H. Yamashita, H. Yu, H. Li, Z. Bian, Photocatalytic dissolution of precious metals by TiO<sub>2</sub> through photogenerated free radicals, *Angew. Chem. Int. Ed.* 61 (2022) e202213640, <https://doi.org/10.1002/ange.202213640>.
- [27] Y. Chen, M. Xu, J. Wen, Y. Wan, Q. Zhao, X. Cao, Y. Ding, Z.L. Wang, H. Li, Z. Bian, Selective recovery of precious metals through photocatalysis, *Nat. Sustain.* 4 (2021) 618–626, <https://doi.org/10.1038/s41893-021-00697-4>.
- [28] H. Shang, Y. Chen, S. Guan, Y. Wang, J. Cao, X. Wang, H. Li, Z. Bian, Scalable and selective gold recovery from end-of-life electronics, *Nat. Chem. Eng.* 1 (2024) 170–179, <https://doi.org/10.1038/s44286-023-00026-w>.
- [29] S. Bingham, W.A. Daoud, Recent advances in making nano-sized TiO<sub>2</sub> visible-light active through rare-earth metal doping, *J. Mater. Chem.* 21 (2011) 2041–2050, <https://doi.org/10.1039/C0JM02271C>.
- [30] G. Chen, T. Wang, J. Zhang, P. Liu, H. Sun, X. Zhuang, M. Chen, X. Feng, Accelerated hydrogen evolution kinetics on NiFe-layered double hydroxide electrocatalysts by tailoring water dissociation active sites, *Adv. Mater.* 30 (2018) 1706279, <https://doi.org/10.1002/adma.201706279>.
- [31] Z. Hou, Z. Sun, C. Cui, D. Zhu, Y. Yang, T. Zhang, Ru coordinated ZnIn<sub>2</sub>S<sub>4</sub> triggers local lattice-strain engineering to endow high-efficiency electrocatalyst for advanced Zn-air batteries, *Adv. Funct. Mater.* 32 (2022) 2110572, <https://doi.org/10.1002/adfm.202110572>.
- [32] M. Marsman, G. Kresse, Relaxed core projector-augmented-wave method, *J. Chem. Phys.* 125 (2006) 104101, <https://doi.org/10.1063/1.2338035>.
- [33] G. Kresse, J. Furthmüller, Efficient iterative schemes for ab initio total-energy calculations using a plane-wave basis set, *Phys. Rev. B* 54 (1996) 11169–11186, <https://doi.org/10.1103/PhysRevB.54.11169>.
- [34] P.E. Blöchl, Projector augmented-wave method, *Phys. Rev. B* 50 (1994) 17953–17979, <https://doi.org/10.1103/PhysRevB.50.17953>.
- [35] A.-R. Allouche, Gabedit—a graphical user interface for computational chemistry softwares, *J. Comput. Chem.* 32 (2011) 174–182, <https://doi.org/10.1002/jcc.21600>.
- [36] H.J. Monkhorst, J.D. Pack, Special points for Brillouin-zone integrations, *Phys. Rev. B* 13 (1976) 5188–5192, <https://doi.org/10.1103/PhysRevB.13.5188>.
- [37] W.-K. Chong, B.-J. Ng, C.-C. Er, L.-L. Tan, S.-P. Chai, Insights from density functional theory calculations on heteroatom P-doped ZnIn<sub>2</sub>S<sub>4</sub> bilayer nanosheets with atomic-level charge steering for photocatalytic water splitting, *Sci. Rep.* 12 (2022) 1927, <https://doi.org/10.1038/s41598-022-05740-8>.
- [38] X. Shi, C. Dai, X. Wang, J. Hu, J. Zhang, L. Zheng, L. Mao, H. Zheng, M. Zhu, Protruding Pt single-sites on hexagonal ZnIn<sub>2</sub>S<sub>4</sub> to accelerate photocatalytic hydrogen evolution, *Nat. Commun.* 13 (2022) 1287, <https://doi.org/10.1038/s41467-022-28995-1>.
- [39] A. Rajan, M.D. Dhileepan, S. Kamalakannan, M. Prakash, S. Krishnamurthy, B. Neppolian, Delineating the role of vacancy defects in increasing photocatalytic hydrogen production in an amorphous metal-organic framework coordinated graphitic carbon nitride, *ACS Appl. Energy Mater.* 6 (2023) 9207–9217, <https://doi.org/10.1021/acsam.3c00581>.
- [40] Y. Yu, G. Chen, G. Wang, Z. Lv, Visible-light-driven ZnIn<sub>2</sub>S<sub>4</sub>/CdIn<sub>2</sub>S<sub>4</sub> composite photocatalyst with enhanced performance for photocatalytic H<sub>2</sub> evolution, *Int. J. Hydrog. Energy* 38 (2013) 1278–1285, <https://doi.org/10.1016/j.ijhydene.2012.11.020>.
- [41] S. Shen, J. Chen, X. Wang, L. Zhao, L. Guo, Microwave-assisted hydrothermal synthesis of transition-metal doped ZnIn<sub>2</sub>S<sub>4</sub> and its photocatalytic activity for hydrogen evolution under visible light, *J. Power Sources* 196 (2011) 10112–10119, <https://doi.org/10.1016/j.jpowsour.2011.08.103>.

- [42] S. Adhikari, A.V. Charanpahari, G. Madras, Solar-light-driven improved photocatalytic performance of hierarchical  $\text{ZnIn}_2\text{S}_4$  architectures, *ACS Omega* 2 (2017) 6926–6938, <https://doi.org/10.1021/acsomega.7b01329>.
- [43] T. Soltani, B.K. Lee, Novel and facile synthesis of Ba-doped  $\text{BiFeO}_3$  nanoparticles and enhancement of their magnetic and photocatalytic activities for complete degradation of benzene in aqueous solution, *J. Hazard. Mater.* 316 (2016) 122–133, <https://doi.org/10.1016/j.jhazmat.2016.03.052>.
- [44] J. Qin, Q. Zhao, Y. Zhao, Y. Wu, B. Pan, C. Wang, Metal-free phosphorus-doped  $\text{ZnIn}_2\text{S}_4$  nanosheets for enhanced photocatalytic  $\text{CO}_2$  reduction, *J. Phys. Chem. C* 125 (2021) 23813–23820, <https://doi.org/10.1021/acs.jpcc.1c07651>.
- [45] Y. Bao, K. Chen,  $\text{AgCl/Ag/g-C}_3\text{N}_4$  hybrid composites: preparation, visible light-driven photocatalytic activity and mechanism, *Nano Micro Lett.* 8 (2016) 182–192, <https://doi.org/10.1007/s40820-015-0076-y>.
- [46] P. Bhavani, D. Praveen Kumar, M. Hussain, T.M. Aminabhavi, Y.-K. Park, Eco-friendly rice husk derived biochar as a highly efficient noble metal-free cocatalyst for high production of  $\text{H}_2$  using solar light irradiation, *Chem. Eng. J.* 434 (2022) 134743, <https://doi.org/10.1016/j.cej.2022.134743>.
- [47] P. Bhavani, D. Praveen Kumar, A. Putta Rangappa, Y. Hong, M. Gopannagari, D. Amaranatha Reddy, T. Kyu Kim, Skeletal  $\text{Cu}_2\text{S}_4$  nanocages wrapped by few-layered black phosphorus nanosheets as an efficient  $\text{H}_2$  production photocatalyst, *ChemCatChem* 13 (2021) 304–312, <https://doi.org/10.1002/cctc.202001111>.
- [48] Q. Wang, W. Wang, L. Zhong, D. Liu, X. Cao, F. Cui, Oxygen vacancy-rich 2D/2D  $\text{BiOCl/g-C}_3\text{N}_4$  ultrathin heterostructure nanosheets for enhanced visible-light-driven photocatalytic activity in environmental remediation, *Appl. Catal. B Environ.* 220 (2018) 290–302, <https://doi.org/10.1016/j.apcatb.2017.08.049>.
- [49] X. Li Li, X. Jing Wang, J. Yu Zhu, Y. Pei Li, J. Zhao, F. Tang Li, Fabrication of two-dimensional  $\text{Ni}_2\text{P/ZnIn}_2\text{S}_4$  heterostructures for enhanced photocatalytic hydrogen evolution, *Chem. Eng. J.* 353 (2018) 15–24, <https://doi.org/10.1016/j.cej.2018.07.107>.
- [50] Y. Yu, W. Yan, X. Wang, P. Li, W. Gao, H. Zou, S. Wu, K. Ding, Surface engineering for extremely enhanced charge separation and photocatalytic hydrogen evolution on  $\text{g-C}_3\text{N}_4$ , *Adv. Mater.* 30 (2018) 1705060, <https://doi.org/10.1002/adma.201705060>.
- [51] Z. Zhang, K. Liu, Z. Feng, Y. Bao, B. Dong, Hierarchical sheet-on-sheet  $\text{ZnIn}_2\text{S}_4/\text{g-C}_3\text{N}_4$  heterostructure with highly efficient photocatalytic  $\text{H}_2$  production based on photoinduced interfacial charge transfer, *Sci. Rep.* 6 (1) (2016) 10, <https://doi.org/10.1038/srep19221>.
- [52] S. Si, H. Shou, Y. Mao, X. Bao, G. Zhai, K. Song, Z. Wang, P. Wang, Y. Liu, Z. Zheng, Y. Dai, L. Song, B. Huang, H. Cheng, Low-coordination single Au atoms on ultrathin  $\text{ZnIn}_2\text{S}_4$  nanosheets for selective photocatalytic  $\text{CO}_2$  reduction towards  $\text{CH}_4$ , *Angew. Chem. Int. Ed.* 61 (2022) e202209446, <https://doi.org/10.1002/anie.202209446>.
- [53] G.-X. Ge, H.-X. Yan, Q. Jing, Y.-H. Luo, Theoretical study of hydrogen adsorption on ruthenium clusters, *J. Clust. Sci.* 22 (2011) 473, <https://doi.org/10.1007/s10876-011-0395-1>.
- [54] Y. Qin, H. Li, J. Lu, Y. Feng, F. Meng, C. Ma, Y. Yan, M. Meng, Synergy between van der Waals heterojunction and vacancy in  $\text{ZnIn}_2\text{S}_4/\text{g-C}_3\text{N}_4$  2D/2D photocatalysts for enhanced photocatalytic hydrogen evolution, *Appl. Catal. B Environ.* 277 (2020) 119254, <https://doi.org/10.1016/j.apcatb.2020.119254>.
- [55] W. Pudkon, S. Kaowphong, S. Pattison, P.J. Miedziak, H. Bahrui, T.E. Davies, D. J. Morgan, G.J. Hutchings, Microwave synthesis of  $\text{ZnIn}_2\text{S}_4/\text{WS}_2$  composites for photocatalytic hydrogen production and hexavalent chromium reduction, *Catal. Sci. Technol.* 9 (2019) 5698–5711, <https://doi.org/10.1039/c9cy01553a>.
- [56] Y. Chen, G. Tian, Z. Ren, K. Pan, Y. Shi, J. Wang, H. Fu, Hierarchical core-shell carbon nanofiber@ $\text{ZnIn}_2\text{S}_4$  composites for enhanced hydrogen evolution performance, *ACS Appl. Mater. Interfaces* 6 (2014) 13841–13849, <https://doi.org/10.1021/am5032083>.
- [57] S. Akbayrak, S. Özkaz, Ruthenium(0) nanoparticles supported on multiwalled carbon nanotube as highly active catalyst for hydrogen generation from ammonia–borane, *ACS Appl. Mater. Interfaces* 4 (2012) 6302–6310, <https://doi.org/10.1021/am3019146>.
- [58] S. Zhang, Z. Zhang, Y. Si, B. Li, F. Deng, L. Yang, X. Liu, W. Dai, S. Luo, Gradient hydrogen migration modulated with self-adapting S vacancy in copper-doped  $\text{ZnIn}_2\text{S}_4$  nanosheet for photocatalytic hydrogen evolution, *ACS Nano* 15 (2021) 15238–15248, <https://doi.org/10.1021/acsnano.1c05834>.
- [59] Q. Zhang, J. Zhang, X. Wang, L. Li, Y.-F. Li, W.-L. Dai, In–N–in sites boosting interfacial charge transfer in carbon-coated hollow tubular  $\text{In}_2\text{O}_3/\text{ZnIn}_2\text{S}_4$  heterostructure derived from In-MOF for enhanced photocatalytic hydrogen evolution, *ACS Catal.* 11 (2021) 6276–6289, <https://doi.org/10.1021/acscatal.0c05520>.
- [60] T. Su, C. Men, L. Chen, B. Chu, X. Luo, H. Ji, J. Chen, Z. Qin, Sulfur vacancy and  $\text{Ti}_3\text{C}_2\text{T}_x$  cocatalyst synergistically boosting interfacial charge transfer in 2D/2D  $\text{Ti}_3\text{C}_2\text{T}_x/\text{ZnIn}_2\text{S}_4$  heterostructure for enhanced photocatalytic hydrogen evolution, *Adv. Sci.* 9 (2022) 2103715, <https://doi.org/10.1002/adv.202103715>.
- [61] Y.-C. Nie, F. Yu, L.-C. Wang, Q.-J. Xing, X. Liu, Y. Pei, J.-P. Zou, W.-L. Dai, Y. Li, S. L. Suib, Photocatalytic degradation of organic pollutants coupled with simultaneous photocatalytic  $\text{H}_2$  evolution over graphene quantum dots/Mn–N– $\text{TiO}_2/\text{g-C}_3\text{N}_4$  composite catalysts: performance and mechanism, *Appl. Catal. B Environ.* 227 (2018) 312–321, <https://doi.org/10.1016/j.apcatb.2018.01.033>.
- [62] W. Zhong, D. Gao, H. Yu, J. Fan, J. Yu, Novel amorphous  $\text{NiCuSx}$   $\text{H}_2$ -evolution cocatalyst: optimizing surface hydrogen desorption for efficient photocatalytic activity, *Chem. Eng. J.* 419 (2021) 129652, <https://doi.org/10.1016/j.cej.2021.129652>.
- [63] S. Zong, L. Tian, X. Guan, C. Cheng, J. Shi, L. Guo, Photocatalytic overall water splitting without noble-metal: decorating CoP on Al-doped  $\text{SrTiO}_3$ , *J. Colloid Interface Sci.* 606 (2022) 491–499, <https://doi.org/10.1016/j.jcis.2021.08.049>.
- [64] L.J. Zhang, R. Zheng, S. Li, B.K. Liu, D.J. Wang, L.L. Wang, T.F. Xie, Enhanced photocatalytic  $\text{H}_2$  generation on cadmium sulfide nanorods with cobalt hydroxide as cocatalyst and insights into their photogenerated charge transfer properties, *ACS Appl. Mater. Interfaces* 6 (2014) 13406–13412, <https://doi.org/10.1021/am501216b>.
- [65] S. Saha, G. Das, J. Thote, R. Banerjee, Photocatalytic metal–organic framework from CdS quantum dot incubated luminescent metallohydrogel, *J. Am. Chem. Soc.* 136 (2014) 14845–14851, <https://doi.org/10.1021/ja509019k>.
- [66] D. Praveen Kumar, A. Putta Rangappa, K.H. Do, Y. Hong, M. Gopannagari, K. Arun Joshi Reddy, P. Bhavani, D. Amaranatha Reddy, T. Kyu Kim, Noble metal free few-layered perovskite-based  $\text{Ba}_2\text{NbFeO}_6$  nanostructures on exfoliated  $\text{g-C}_3\text{N}_4$  layers as highly efficient catalysts for enhanced solar fuel production, *Appl. Surf. Sci.* 572 (2022) 151406, <https://doi.org/10.1016/j.apsusc.2021.151406>.
- [67] Y. Xiao, G. Tian, W. Li, Y. Xie, B. Jiang, C. Tian, D. Zhao, H. Fu, Molecule self-assembly synthesis of porous few-layer carbon nitride for highly efficient photoredox catalysis, *J. Am. Chem. Soc.* 141 (2019) 2508–2515, <https://doi.org/10.1021/jacs.8b12428>.
- [68] S. Manchala, V.S.R.K. Tandava, L.R. Nagappagari, S. Muthukonda Venkatakrishnan, D. Jampaiah, Y.M. Sabri, S.K. Bhargava, V. Shanker, Fabrication of a novel  $\text{ZnIn}_2\text{S}_4/\text{g-C}_3\text{N}_4$ /graphene ternary nanocomposite with enhanced charge separation for efficient photocatalytic  $\text{H}_2$  evolution under solar light illumination, *Photochem. Photobiol. Sci.* 18 (2019) 2952–2964, <https://doi.org/10.1039/c9pp00234k>.
- [69] A. Wang, S. Wu, J. Dong, R. Wang, J. Wang, J. Zhang, S. Zhong, S. Bai, Interfacial facet engineering on the Schottky barrier between plasmonic Au and  $\text{TiO}_2$  in boosting the photocatalytic  $\text{CO}_2$  reduction under ultraviolet and visible light irradiation, *Chem. Eng. J.* 404 (2021) 127145, <https://doi.org/10.1016/j.cej.2020.127145>.